



# Supercontinuum generation in seven-core fibers

A. ANTIKAINEN<sup>1,\*</sup>  AND G. P. AGRAWAL<sup>1,2</sup> <sup>1</sup>The Institute of Optics, University of Rochester, Rochester, New York 14627, USA<sup>2</sup>Laboratory for Laser Energetics, 250 East River Rd, Rochester, New York 14623, USA

\*Corresponding author: aku.antikainen@rochester.edu

Received 24 June 2019; revised 26 August 2019; accepted 2 September 2019; posted 4 September 2019 (Doc. ID 370837); published 3 October 2019

**We present a detailed numerical study of supercontinuum generation in hexagonal seven-core fibers with single-core input in the short pulse regime. Important spectral broadening mechanisms are shown to result from or strongly depend on the frequency dependence of linear coupling between the cores. Namely, soliton supermode transitions, inter-supermodal four-wave mixing, and inter-supermodal dispersive wave generation are among the key nonlinear phenomena specific to multi-core fibers, and their relative importance is heavily dependent on core separation.** © 2019 Optical Society of America

<https://doi.org/10.1364/JOSAB.36.002927>

## 1. INTRODUCTION

Supercontinuum generation inside single-mode fibers is a well understood phenomenon [1]. Since 2012, the nonlinear effects in graded-index multi-mode fibers have been studied extensively [2–4]. More recently, step-index multi-mode fibers have been shown to exhibit interesting nonlinear phenomena unobservable in graded-index fibers [5,6]. Multi-core fibers have been considered a promising platform for optical communication systems due to their ability to suppress detrimental nonlinear effects and because of the remarkable ability of an  $N$ -core fiber to outperform an equivalent communication link of  $N$  single-mode fibers [7–10]. However, multi-core fibers and other arrays of coupled waveguides do support nonlinear optical phenomena such as a discrete analog of self-focusing [11] and nonlinear pulse combining [12]. The intensity-dependent transmission characteristics of coupled waveguides can also be utilized for applications such as nonlinear optical switching [13,14] and pulse compression [15]. Multi-core fibers are capable of delivering high-energy pulses by distributing their energy among several cores through the excitation of the so-called supermodes.

One of the most common types of multi-core fibers is the hexagonal seven-core fiber. Such fibers have been used for supercontinuum generation [16–23]. However, the fibers in these previous studies have been photonic crystal fibers where the nonlinearities are enhanced due to a small mode area, and the dispersion has been carefully engineered to facilitate the generation of new frequency components over a broad wavelength range. Tapering has been used to further amplify nonlinear effects for broader supercontinuum spectra [21]. In this paper, we consider a step-index seven-core fiber and numerically show that supercontinuum generation can take place even in such a regular multi-core fiber without dispersion engineering. The

emphasis is on the effect of core separation on the width of the resulting output spectra, and we detail the dependence of the spectral width on core separation in the short pulse regime using a 100 fs input pulse. Both center-core and outer-core excitation are considered. Different regimes of spectral broadening are identified and shown to be connected to various nonlinear phenomena, some of which are specific to multi-core fibers [24].

The paper is organized as follows. In the first section, we go through the linear propagation characteristics of a seven-core fiber and introduce the full propagation equation including nonlinear effects and also the numerical method to solve the equation used in this study. In the next section we consider supercontinuum generation in a seven-core fiber when the center core is used as the input, and in the section after that, we switch to using an outer core as the input core.

## 2. PULSE PROPAGATION IN A MULTI-CORE FIBER

The fiber considered here is a hexagonal, seven-core fiber with one central core and six outer cores arranged in a regular hexagonal pattern around the center core. The diameter of the cores is 6  $\mu\text{m}$  and the nearest-neighbor center-to-center spacing between the cores is varied from 12  $\mu\text{m}$  to 30  $\mu\text{m}$  to modify the strength of linear coupling. All cores of the fiber support a single mode near the 1.55  $\mu\text{m}$  wavelength.

It is customary and mathematically convenient to consider only one polarization and to describe the pulse propagation through the concept of pulse envelope. Namely, we write the electric field in the vicinity of a single core as

$$\mathbf{E}(\mathbf{r}, t) = \Re\{e^{i\mathbf{p}\cdot\mathbf{F}(x, y)} A(z, t) \exp(i\beta_0 z - i\omega_0 t)\}, \quad (1)$$

where  $\hat{\mathbf{p}}$  is the unit vector in the direction of polarization,  $F(x, y)$  is the transverse field profile of the single mode of the core,  $A(z, t)$  is the envelope,  $\omega_0$  is the carrier frequency, and  $\beta_0$  is the propagation constant at this frequency. It is common to choose the carrier frequency  $\omega_0$  to be the central frequency of the optical pulse to ensure that  $A(z, t)$  is a slowly evolving function of  $z$ . This *slowly evolving wave approximation* makes it possible to neglect the  $\partial^2 A(z, t)/\partial z^2$  term arising from Maxwell's equations when deriving the propagation equation for the envelope  $A(z, t)$ . The derivation of the underlying nonlinear Schrödinger equation (NLSE) for  $A(z, t)$  in the case of a single-core fiber can be found in literature [25–27]. The multi-core counterpart of the equation includes linear coupling between the cores and can be written in the following form in the frequency domain:

$$\begin{aligned} \frac{\partial \tilde{A}_p(z, \omega)}{\partial z} = & i [\beta(\omega) - \beta_0 - \beta_1(\omega - \omega_0)] \tilde{A}_p(z, \omega) \\ & + i\gamma(\omega)\mathcal{F} \left\{ [R(t) * |A_p(z, t)|^2] A_p(z, t) \right\} (\omega) \\ & + i \sum_{l \neq p} \kappa_{pl}(\omega) \tilde{A}_l(z, \omega), \end{aligned} \quad (2)$$

where  $A_p(z, t)$  is the temporal envelope of the field in the  $p^{\text{th}}$  core, and  $\tilde{A}_p(z, \omega)$  is its Fourier transform defined as

$$\tilde{A}_p(z, \omega) = \mathcal{F}\{A_p(z, t)\}(\omega) = \int_{-\infty}^{\infty} A_p(z, t) e^{i\omega t} dt. \quad (3)$$

The first term in the square brackets on the right side in Eq. (2) accounts for dispersive effects through  $\beta(\omega)$ . The subtraction of  $\beta_0 = \beta(\omega_0)$  and  $\beta_1 = [d\beta/d\omega]_{\omega=\omega_0}$  from  $\beta(\omega)$  implies that the frame of reference moves at the group velocity of the input pulse, i.e., the time  $t$  is with respect to the temporal location of the center of the input pulse in an isolated core in the absence of nonlinearities. The nonlinear response function is  $R(t) = (1 - f_R)\delta(t) + f_R b_R(t)$ , and it includes the Kerr and Raman effects with a Raman fraction of  $f_R = 0.18$ . The Raman response function  $b_R(t)$  is calculated in the frequency domain using the experimental Raman data for fused silica [28]. The nonlinear parameter  $\gamma(\omega) = n_2\omega/[cA_{\text{eff}}(\omega)]$  is determined by using  $n_2 = 3.2 \cdot 10^{-20} \text{ m}^2/\text{W}$  and computing the fundamental mode effective area for each frequency in an isolated core. Inter-core nonlinear interactions have not been included in Eq. (2), but we have verified that their omission is justified by performing example simulations with inter-core nonlinearities taken into account. The inter-core terms are largest for the smallest core separation (12  $\mu\text{m}$  in this study), but even for this smallest core separation, the largest inter-core nonlinear terms are less than 0.7% of the dominant intra-core terms, and thus they can safely be left out. Contrary to a common misconception,  $A(z, t)$  does not need to be a slowly varying function of  $t$  if certain other conditions are satisfied [25]. Without going into the details, we point out that these conditions are satisfied for silica fibers in the wavelength range from visible to mid-infrared, and the validity of Eq. (2) will not be compromised even if its numerical solutions were to contain single-cycle optical pulses.

Equation (2) can be rewritten as a vector equation:

$$\begin{aligned} \frac{\partial \tilde{\mathbf{A}}(z, \omega)}{\partial z} = & i\mathbf{M}(\omega)\tilde{\mathbf{A}}(z, \omega) \\ & + i\gamma(\omega)\mathcal{F} \left\{ [R(t) * |\mathbf{A}(z, t)|^2] \mathbf{A}(z, t) \right\} (\omega), \end{aligned} \quad (4)$$

where  $\mathbf{A}(z, \omega)$  is a vector consisting of the envelopes of the fields in each core, and the matrix  $\mathbf{M}$  describes all the linear effects. The diagonal elements of  $\mathbf{M}$  are  $\beta(\omega) - \beta_0 - \beta_1(\omega - \omega_0)$  and describe dispersion, whereas the off-diagonal elements are responsible for coupling between the cores. Generally all the off-diagonal elements of  $\mathbf{M}$  are non-zero but the dominant contribution comes from the coupling between neighboring cores. When the center-to-center core separation is 12  $\mu\text{m}$ , the nearest-neighbor coupling terms are larger than the other terms by a factor of 60 or more in the wavelength range 1–2.5  $\mu\text{m}$ .

Before solving Eq. (4) numerically for studying supercontinuum generation, we need to know the frequency dependence of both the propagation constant  $\beta(\omega)$  and the coupling coefficient  $\kappa_{pl}(\omega)$  appearing in Eq. (2) over the entire spectral range of the calculated spectra. For this purpose, we use the well-known Sellmeier equation for the cladding's refractive index  $n_2(\lambda)$  for fused silica [29]:

$$\begin{aligned} n_2(\lambda) = & \left[ 1 + \frac{0.6961663\lambda^2}{\lambda^2 - 0.0684043^2} \right. \\ & \left. + \frac{0.4079426\lambda^2}{\lambda^2 - 0.1162414^2} + \frac{0.8974794\lambda^2}{\lambda^2 - 9.896161^2} \right]^{1/2}, \end{aligned} \quad (5)$$

where  $\lambda$  is in micrometers. The refractive index of the cores is taken to be  $n_1(\lambda) = n_2(\lambda) + 0.01$  across the whole wavelength range.

Using the known core radius and the refractive indices of the core and cladding materials, the propagation constant  $\beta(\omega)$  of an isolated core can be computed by assuming an infinite cladding and matching the tangential fields at the core-cladding boundary. The field profile of the fundamental mode in an isolated core was used to calculate the frequency dependence of the effective mode area  $A_{\text{eff}}(\omega)$ , which was in turn used to calculate the nonlinear parameter  $\gamma(\omega)$  appearing in Eq. (4). To give a numerical example, the nonlinear parameter at the center wavelength of 1.55  $\mu\text{m}$  for our multicore fiber is  $\gamma(\omega_0) = 3.27 \text{ (kmW)}^{-1}$ .

The frequency dependence of the coupling coefficient  $\kappa_{pl}(\omega)$  can also be calculated by integrating over the mode profile. We have found it convenient to use the following simple analytic formula for the coupling between two neighboring cores [30]:

$$\kappa(\omega) = \frac{\pi}{2an_1} \sqrt{n_1^2 - n_2^2} \exp[-(c_0 + c_1\bar{d} + c_2\bar{d}^2)], \quad (6)$$

where  $a$  is the core radius, and  $\bar{d} \equiv d/a$  is the normalized center-to-center spacing between the two cores. The constants  $c_0$ ,  $c_1$ , and  $c_2$  depend on the  $V$  parameter defined as  $V(\omega) = (a\omega/c)\sqrt{n_1^2 - n_2^2}$  as

$$\begin{aligned}
 c_0 &= 5.2789 - 3.663V + 0.3841V^2, \\
 c_1 &= -0.7769 + 1.2252V - 0.0152V^2, \\
 c_2 &= -0.0175 - 0.0064V + 0.0009V^2.
 \end{aligned} \quad (7)$$

This relation is accurate to within 1% for values of  $V$  and  $\bar{d}$  in the range  $1.5 \leq V \leq 2.5$  and  $2 \leq \bar{d} \leq 4.5$ . While it is customary to approximate the fundamental mode field profile with a Gaussian, the Gaussian approximation becomes very inaccurate further into the cladding. The derivation of the approximate formula of Eq. (6) is based on the more accurate Gaussian-exponential-Hankel approximation of the fundamental mode [31].

### 3. SUPERMODES OF A MULTI-CORE FIBER

It is well known that when the cores of a multi-core fiber are so close that the coupling among them is not negligible, one must consider the supermodes of the whole structure, which represent the true modes of such a fiber. It turns out that these supermodes are required for a proper understanding of the nonlinear effects. When the coupling is restricted to the two nearest neighbors, the supermodes are easy to determine analytically, but the same can also be done when accounting for all couplings terms.

The first part of Fig. 1 shows the scheme used to number the seven cores of the fiber as well as the letter labels for the supermodes. We denote the center core as the first core, and the six outer cores are numbered from 2 to 7 as shown. The matrix  $M(\omega)$  for this configuration takes the form

$$M(\omega) = [\beta(\omega) - \beta_0 - \beta_1(\omega - \omega_0)] I_7 + \kappa(\omega)K, \quad (8)$$

where  $I_7$  is the  $7 \times 7$  identity matrix,  $\kappa(\omega)$  is the frequency-dependent nearest-neighbor coupling, and the constant matrix  $K$  has the form

$$K = \begin{bmatrix} 0 & 1 & 1 & 1 & 1 & 1 & 1 \\ 1 & 0 & 1 & 0 & 0 & 0 & 1 \\ 1 & 1 & 0 & 1 & 0 & 0 & 0 \\ 1 & 0 & 1 & 0 & 1 & 0 & 0 \\ 1 & 0 & 0 & 1 & 0 & 1 & 0 \\ 1 & 0 & 0 & 0 & 1 & 0 & 1 \\ 1 & 1 & 0 & 0 & 0 & 1 & 0 \end{bmatrix}. \quad (9)$$

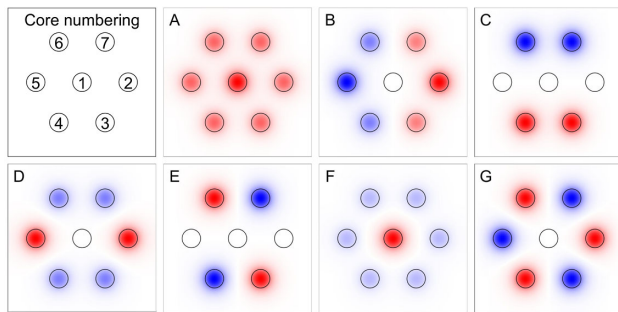


**Fig. 1.** Numbering scheme and supermode field patterns at a wavelength of  $1.55 \mu\text{m}$  for a seven-core fiber. Core diameter is  $6 \mu\text{m}$ , and the center-to-center spacing is  $15 \mu\text{m}$ . The colors represent field values from  $-1$  (blue) to  $+1$  (red).

This matrix reflects the fact that the center core is coupled to all other cores while the outer cores are coupled to three neighboring cores with the same spacing.

In the absence of nonlinearities (i.e., for weak fields), Eq. (4) becomes a linear equation:

$$\frac{\partial \tilde{\mathbf{A}}(z, \omega)}{\partial z} = iM(\omega)\tilde{\mathbf{A}}(z, \omega). \quad (10)$$

This equation can be reduced to the eigenvalue equation  $(M - \beta^s I_7)\tilde{\mathbf{A}}(z, \omega) = 0$  by assuming that  $\tilde{\mathbf{A}}(z, \omega) = \tilde{\mathbf{A}}_0(\omega)e^{i\beta^s(\omega)z}$  is a solution of Eq. (10). Here,  $\tilde{\mathbf{A}}_0(\omega)$  is an eigenvector of  $M(\omega)$  corresponding to the eigenvalue  $\beta^s(\omega)$ . Because  $\tilde{\mathbf{A}}_0(\omega)$  is constant along  $z$ , such solutions of Eq. (10) describe fields that propagate unchanged except for their phase that evolves as  $e^{i\beta^s(\omega)z}$ . These are the supermodes of the multi-core fiber, and  $\beta^s(\omega)$  are the propagation constants of these supermodes. Since  $M$  is a  $7 \times 7$  matrix, there are seven supermodes.

Owing to the specific form of the matrix  $M$  in Eq. (8), we need to find only the eigenvalues and eigenvectors of the matrix  $K$ . As these quantities do not depend on the frequency  $\omega$ , the problem is simplified considerably. The seven eigenvalues of the matrix  $K$  are found to be, in decreasing order,  $1 + \sqrt{7}$ ,  $1$ ,  $1$ ,  $-1$ ,  $-1$ ,  $1 - \sqrt{7}$ , and  $-2$ . Using them, the supermode propagation constants are given by

$$\begin{aligned}
 \beta^A(\omega) &= \beta(\omega) + (1 + \sqrt{7})\kappa(\omega), \\
 \beta^B(\omega) &= \beta(\omega) + \kappa(\omega), \\
 \beta^C(\omega) &= \beta(\omega) + \kappa(\omega), \\
 \beta^D(\omega) &= \beta(\omega) - \kappa(\omega), \\
 \beta^E(\omega) &= \beta(\omega) - \kappa(\omega), \\
 \beta^F(\omega) &= \beta(\omega) + (1 - \sqrt{7})\kappa(\omega), \\
 \beta^G(\omega) &= \beta(\omega) - 2\kappa(\omega),
 \end{aligned} \quad (11)$$

where the superscript letters denote different supermodes, and the propagation constants have been written in the laboratory coordinates as opposed to the input pulse's frame of reference. The supermodes  $B$  and  $C$  have the same propagation constants, as do  $D$  and  $E$  (two-fold degeneracy).

The eigenvectors corresponding to different supermodes give the relative field amplitudes in each core, and the supermode field patterns can therefore be determined through the corresponding linear combinations of the fields in the seven cores. Using the notation  $F^s(x, y) = \sum_{j=1}^7 b_j^s F_j(x, y)$ , where  $F_j(x, y)$  is the mode distribution of the  $j$ th core and  $b_j^s$  are the expansion coefficients for the  $s$ th supermode, the coefficients  $b_j^s$  can be determined from the eigenvectors of the matrix  $K$ . The eigenvectors are given by the columns of the following matrix (ordered from  $A$  to  $G$  from left to right):

$$\begin{bmatrix} \sqrt{7}-1 & 0 & 0 & 0 & 0 & \sqrt{7}+1 & 0 \\ 1 & 2 & 0 & 2 & 0 & -1 & 1 \\ 1 & 1 & 1 & -1 & 1 & -1 & -1 \\ 1 & -1 & 1 & -1 & -1 & -1 & 1 \\ 1 & -2 & 0 & 2 & 0 & -1 & -1 \\ 1 & -1 & -1 & -1 & 1 & -1 & 1 \\ 1 & 1 & -1 & -1 & -1 & -1 & -1 \end{bmatrix}. \quad (12)$$

As mentioned earlier, these eigenvectors are independent of wavelength as well as core separation, a feature that simplifies the problem considerably. They can be used to construct the field patterns of the supermodes, and these patterns are shown in Fig. 1, with the letters marking different supermodes. Supermodes *A* and *F* are the only ones with six-fold symmetry and also the only ones where the center core has appreciable electric field. While hard to see in Fig. 1, the eigenvectors given in Eq. (12) tell us that supermode *F* has some optical power in the outer cores as well, with a field amplitude of  $-1/(\sqrt{7}+1) \approx -0.27$  relative to the center core. The minus sign implies that the fields in the center and outer cores are exactly out of phase with each other.

#### 4. NUMERICAL SCHEME

Equation (2) can be solved numerically using the well-known split-step Fourier method [27], where the nonlinear step and linear step are performed in succession. The nonlinear step must be done in the time domain, with convolutions handled conveniently in the frequency domain. In the context of single-mode fibers, the linear step is usually referred to as the dispersive step, as dispersion is the only linear effect in that case. In the present situation, the linear step includes both dispersion and coupling terms. The linear step is essentially finding  $\tilde{\mathbf{A}}(z+h, \omega)$  from  $\tilde{\mathbf{A}}(z, \omega)$  in the absence of nonlinearities. The linear equation is given in Eq. (10), and its solution  $\tilde{\mathbf{A}}(z+h, \omega)$  is given by

$$\tilde{\mathbf{A}}(z+h, \omega) = e^{ihM(\omega)} \tilde{\mathbf{A}}(z, \omega). \quad (13)$$

Although the linear step is quite simple, mathematically, problems arise when it is implemented numerically. To accurately describe the field  $\tilde{\mathbf{A}}(z, \omega)$ , it has to be represented by a matrix with tens of thousands of columns, each column corresponding to a specific frequency ( $2^{16} = 65536$  columns were used in this study). Because of the frequency dependence of the matrix *M*, taking the linear step requires multiplying a seven-element vector with a  $7 \times 7$  matrix  $2^{16}$  times. The step size *h* also needs to be relatively small (100  $\mu\text{m}$  in this study), and the total number of steps taken is quite large for a few-meter-long fiber. Due to numerous matrix multiplications, the linear step becomes extremely time consuming when performed this way, and accurate numerical simulations become impractical.

A better way to perform the linear step numerically is to first exploit the specific structure of the matrix *M*( $\omega$ ) in Eq. (8). Using it, we can write Eq. (13) as

$$\tilde{\mathbf{A}}(z+h, \omega) = e^{ih\kappa(\omega)K} e^{ih[\beta(\omega)-\beta_0-\beta_1(\omega-\omega_0)]I_7} \tilde{\mathbf{A}}(z, \omega). \quad (14)$$

The dispersive part in the second exponential now reduces to multiplication of each column of  $\tilde{\mathbf{A}}$  by a frequency-dependent scalar because the matrix  $I_7$  is the diagonal identity matrix. This

reflects the fact that all cores are identical. In the simulations, the dispersive part of each linear step reduces to multiplying each row of the  $7 \times 2^{16}$  matrix by a  $2^{16}$  element vector. Even if the cores were not identical, this step would still remain an element-wise multiplication of two  $7 \times 2^{16}$  matrices.

To carry out the coupling part of the linear step, we need to compute  $e^{ih\kappa(\omega)K} \tilde{\mathbf{A}}(z, \omega)$  numerically. We can utilize the fact that each element of the matrix *K* is either zero or 1 and write it as

$$e^{ih\kappa(\omega)K} = (e^{ih\kappa}K)^{\kappa(\omega)} = Q\Lambda^{\kappa(\omega)}Q^T, \quad (15)$$

where we use  $e^{ih\kappa} = Q\Lambda Q^T$ , and where  $\Lambda$  is a diagonal matrix. Using this decomposition, the only matrix that has frequency dependence is a diagonal matrix. Thus, the multiplication of the  $7 \times 2^{16}$  envelope matrix by a frequency-dependent  $7 \times 7$  diagonal matrix can be numerically performed as an element-wise multiplication of two  $7 \times 2^{16}$  matrices. This significantly reduces the computational time of the linear step and makes it feasible to include the frequency dependence of linear coupling in the numerical simulations presented here. Note that the full linear step has to be performed in two stages (dispersion and coupling) because of different frequency dependencies of the dispersion  $\beta(\omega)$  and coupling  $\kappa(\omega)$  parameters. Also note that if coupling between non-neighboring cores were to be included, the matrix *M*( $\omega$ ) would have three different coupling terms (in the hexagonal seven-core fiber case) and could still be decomposed as

$$M(\omega) = [\beta(\omega) - \beta_0 - \beta_1(\omega - \omega_0)]I_7 + \kappa_1(\omega)K_1 + \kappa_2(\omega)K_2 + \kappa_3(\omega)K_3, \quad (16)$$

where  $\kappa_1$ ,  $\kappa_2$ , and  $\kappa_3$  denote different coupling terms between cores at various distances from one another. The same decomposition method could be applied to account for each kind of coupling. This method can also be generalized to other structures, such as linear arrays of coupled waveguides or multi-core fibers with different core arrangements.

#### 5. RESULTS FOR CENTER-CORE EXCITATION

In this section, we study the evolution of an input pulse launched into the central core of the seven-core fiber. This pulse has a width of 100 fs (full width at half maximum, FWHM) with a sech-shape and its central wavelength is taken to be 1.55  $\mu\text{m}$ . Owing to the hexagonal symmetry of the seven-core fiber, the center-core excitation is the simplest to analyze. It can be seen intuitively in Fig. 1 and rigorously from the eigenvectors in (12) that when the center core is used as the input core, only supermodes *A* and *F* are excited with different amplitudes. Furthermore, because of the six-fold symmetry of the input field, the fields in outer cores will be identical to one another under ideal conditions. In practice, small variations that would break the symmetry could have some effect, but we focus here on a near-perfect fiber. It then suffices to study the evolution of the field in the center core and one outer core. Note that this fact can also be utilized to speed up the simulations with simple mathematical manipulations.

To get an idea of the pulse evolution dynamics, we first consider a fiber in which the seven cores are separated by 12  $\mu\text{m}$ .

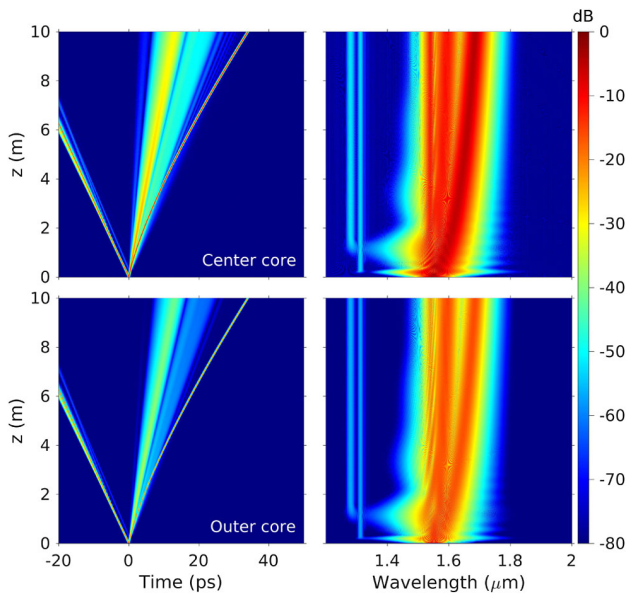


**Fig. 2.** Evolution of a 100 fs input pulse launched with 15 kW peak power into the center core of a seven-core fiber with 12  $\mu\text{m}$  core separation. Top row represents the center core, and the bottom row corresponds to one of the outer cores. The logarithmic color scale ranges from  $-80$  dB to 0. See Visualization 1 for an animated spectrogram of this simulation.

Such a relatively small separation causes the cores to be strongly coupled. Figure 2 shows the temporal and spectral evolutions of a 100 fs pulse launched with 15 kW peak power. Because of relatively strong linear coupling, the two excited supermodes  $A$  and  $F$  have vastly different propagation constants in accordance with Eq. (11). The two supermodes thus quickly separate in time, causing the input pulse to split into two daughter pulses. Both daughter pulses form solitons whose spectra undergo a continuous red shift with distance [32]. Moreover, as the trailing soliton in supermode  $F$  is more intense, it is much narrower and thus red shifts at a faster rate compared to the leading soliton in supermode  $A$ . The differences in the amplitudes of the two solitons can be estimated by noting that  $(7 - \sqrt{7})/14 \approx 31\%$  of the energy is initially in supermode  $A$  and  $(7 + \sqrt{7})/14 \approx 69\%$  in  $F$ . Figure 1 helps us understand the uneven energy distribution between the supermodes. It shows that supermode  $F$  is more concentrated in the center than supermode  $A$ , so more of  $F$  will be needed for a linear combination of  $A$  and  $F$  to yield the total field that has no energy in the outer ones.

While the initial temporal splitting of the input pulse into two daughter pulses in Fig. 2 is due to the frequency dependence of the coupling parameter  $\kappa(\omega)$ , the further evolution of each daughter pulse is similar to the nonlinear evolution in single-mode fibers [1]. The spectrum broadens due to dispersive wave (DW) emission and soliton self-frequency shift, creating a supercontinuum whose width covers a range from 1.3  $\mu\text{m}$  to 1.8  $\mu\text{m}$  with some internal structure. For example, the two peaks at 1.6  $\mu\text{m}$  and 1.68  $\mu\text{m}$  have roughly the same amount of energy in the outer cores, but the 1.68  $\mu\text{m}$  peak is visibly much stronger in the central core. This is a manifestation of the peak at 1.68  $\mu\text{m}$  belonging to the trailing soliton in supermode  $F$ .

The spectral peaks of the DWs in Fig. 2 are at 1.288  $\mu\text{m}$  and 1.313  $\mu\text{m}$ , and the DWs can also be seen as faint lines next to the solitons' trajectories in the temporal trace. Note that the strong lines between the two solitons in the temporal trace are not DWs emitted by solitons but simply pump remnants in supermode  $F$ , which is evident in the spectrogram (see Visualization 1). It is not required that the DWs emitted by the solitons are in the same supermodes as the solitons. Indeed, it was observed that the fields in the outer cores are in phase with the field in the center core for both DWs, which means that they are both in supermode  $A$ . By looking at the spectrogram at various propagation distances (Visualization 1), we can identify the first DW at a propagation distance of 20 cm as being emitted by the trailing soliton and the DW at 1 m as belonging to the leading soliton.

The observed wavelengths of the DWs are close to the predictions of the DW phase-matching condition for solitons. The condition is given by [27]

$$\beta(\omega) - \beta_0 - (\omega - \omega_0)/v_g - \gamma_0 P_0 = 0, \quad (17)$$

where  $\beta_0$  is the propagation constant of the soliton,  $\gamma_0 = 3.2831/(\text{Wkm})$  is the nonlinear parameter at the central wavelength of the soliton, and  $v_g$  is the group velocity of the soliton. To find the wavelength of the DW associated with the trailing soliton using Eq. (17),  $\beta_0$  and  $v_g$  must be taken from the dispersion curve for supermode  $F$ , as that is the supermode of the trailing soliton. Using these values for the parameters in Eq. (17) and keeping in mind that the DWs are in supermode  $A$  gives the DW wavelength as 1.314  $\mu\text{m}$  when  $P_0$  is taken to be the peak power of the trailing soliton in the center core after 20 cm of propagation (14.8 kW). This is close to the observed value of 1.313  $\mu\text{m}$ . The slight discrepancy is likely due to the fact that  $P_0$  is understood to be the peak power in the center core, whereas DW emission also takes place in the outer cores, even if most of the optical power is in the center core. The peak power of the trailing soliton in the outer cores is 1200 W at a propagation distance of 20 cm, which would predict a DW wavelength of 1.305  $\mu\text{m}$ . The observed DW wavelength thus falls between these two predictions but is closer to the center core prediction. The other DW in Fig. 2 is emitted by the leading soliton in supermode  $A$  after approximately 1 m of propagation, at which point the peak power of the leading soliton in the center core is 1560 W, predicting a DW at 1.288  $\mu\text{m}$  and again matching the observations.

One of the defining characteristics of a supercontinuum is its spectral width. To assign a measure to the spectral extent of the structured supercontinuum generated in a seven-core fiber, it is reasonable to use the standard deviation of the total spectrum. Its use allows us to compare spectral widths of different supercontinua with considerable internal structure with peaks and gaps as well as different spatial profiles. The standard deviation  $\sigma$  is defined as

$$\sigma = \sqrt{\int_0^\infty (\nu - \bar{\nu})^2 S(\nu) d\nu}, \quad (18)$$

where  $S(\nu)$  is the spectrum in linear units,  $\nu$  is the optical frequency, and  $\bar{\nu}$  is the spectral center of mass defined as

$$\bar{\nu} = \int_0^\infty \nu S(\nu) d\nu. \quad (19)$$

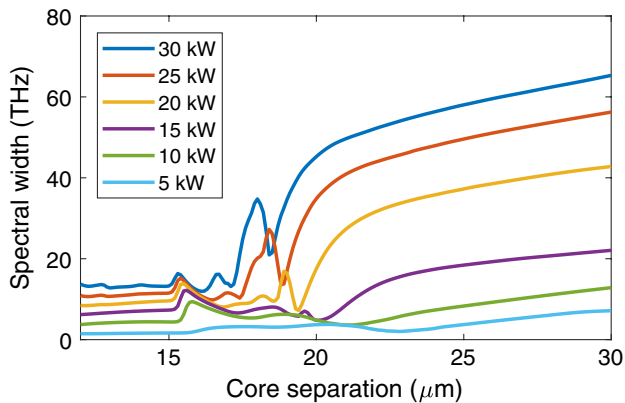
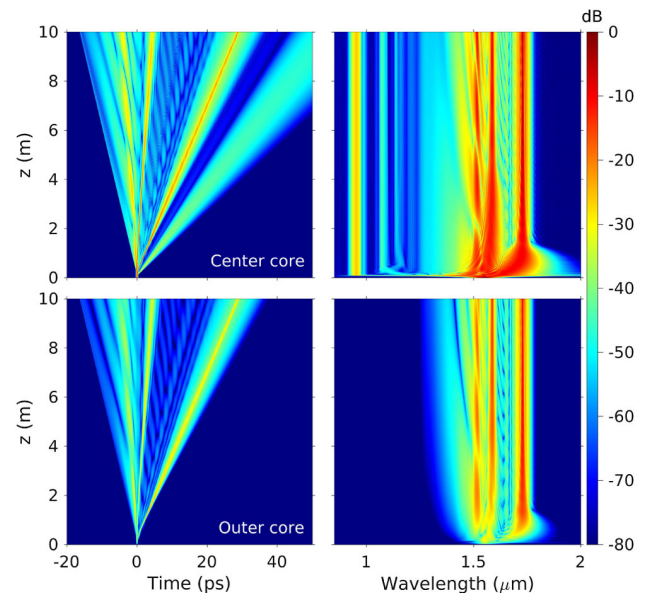


**Fig. 3.** Spectral widths of the supercontinua at the output of the 10-m-long seven-core fiber as a function of core separation. Different curves correspond to different input peak powers of the 100 fs input pulse.

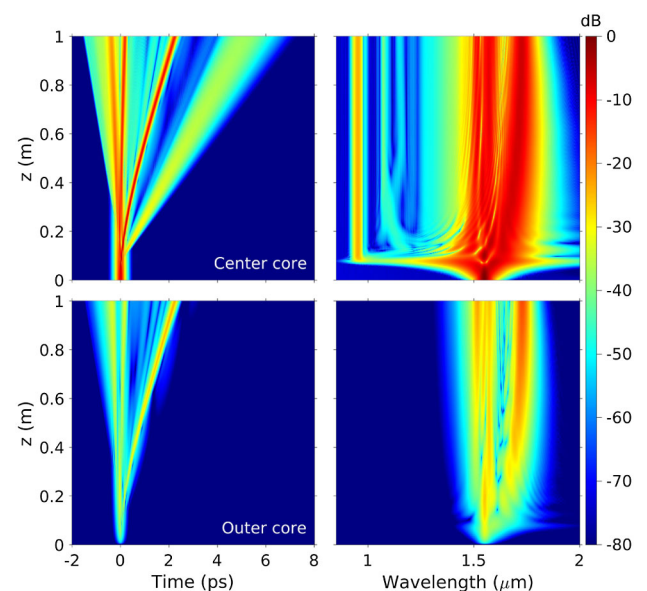
Using this definition, we can compare how the spectral width changes when the input peak power and core separation in the fiber are varied.

Figure 3 shows the widths of the total (all cores combined) output supercontinua as a function of core separation for various input peak powers. Based on the shape of the curves, three distinct regimes can be identified: strong coupling, intermediate coupling, and weak coupling. The strong-coupling region corresponds to core separations  $d < 15 \mu\text{m}$ , while the weak-coupling region occurs for  $d > 20 \mu\text{m}$ . The intermediate-coupling regime lies between these two regions. The strong-coupling region is characterized by relatively small spectral width and an approximately linear dependence on the input power. The broadest spectra occur in the weak-coupling region because the center core then behaves as a nearly isolated core of a single-mode fiber with most of the pulse energy concentrated in the center core alone. Higher optical powers lead to more pronounced nonlinearities, and this enhances spectral broadening, but only if the input power is high enough to start the spectral broadening process to begin with. No appreciable spectral broadening occurs for low input peak powers for any core separation.

As a specific example of the weak-coupling region, Figs. 4 and 5 show the temporal and spectral evolution of the same 15 kW input pulse in a fiber whose cores are separated by  $25 \mu\text{m}$ . Figure 5 shows the first meter of evolution under the same input conditions as Fig. 4 for a better understanding of the effects happening over short length scales during the very initial stages of propagation. The evolution is first similar to that of a pulse in a single-mode fiber, and the forming soliton red shifts rapidly over a short distance. However, the coupling becomes stronger as the spectrum red shifts (owing to the frequency dependence of  $\kappa$ ), and pulse energy starts to spread more and more to the outer cores. Once the coupling has sufficiently increased, energy of the soliton redistributes among the cores, and this together with the fact that  $\gamma(\omega)$  decreases with increasing wavelength brings the red shift to a complete halt [24,33]. The resulting spectrum consists of two widely separated soliton peaks as well as DWs far away and hence the spectral width is large. The initial soliton red shift increases with increasing peak power and core separation.



**Fig. 4.** Evolution of a 100 fs sech pulse launched with 15 kW peak power into the center core of a seven-core fiber with  $25 \mu\text{m}$  core separation. See Visualization 2 for an animated spectrogram of this simulation.



**Fig. 5.** First meter of pulse evolution shown in Fig. 4.

Figure 5 gives a better understanding of the early evolution dynamics when the core separation is large. The first 10 cm are characterized by rapid spectral broadening, and there is a point around 8 cm where the spectrum spans an octave. The spectral broadening is due to the temporal compression of the forming soliton that emerges from the input pulse. Notably, little power is coupled to the outer cores during the initial stages of evolution, and the pulse essentially sees an isolated core. This is also corroborated by the emergence of DWs at much shorter wavelengths (around 958 nm) and only in the center core compared to the cases where the core separation is smaller.

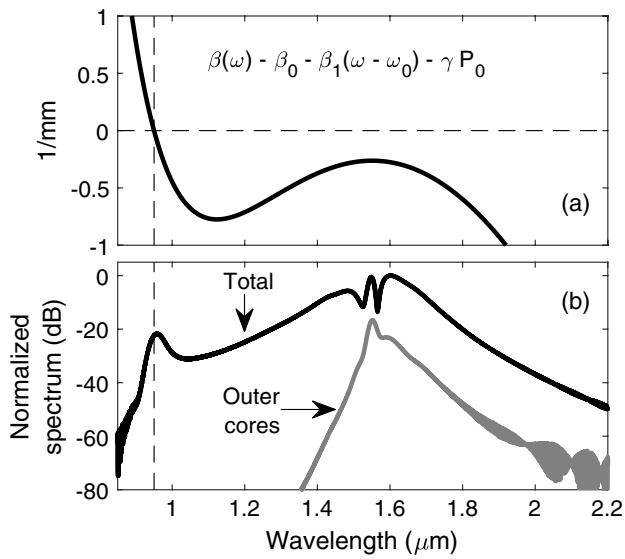


**Fig. 6.** (a) Left side of the phase-matching equation, and (b) spectrum of the 15 kW input pulse after 8 cm of propagation in a fiber where the core separation is 25  $\mu\text{m}$ .

At a propagation distance of 8 cm, the pulse is still heavily confined in the center core, with the outer cores containing only 0.67% of the total energy. The peak power of the temporally compressed pulse is 80 kW, and this value can be used for the phase-matching condition of Eq. (17), the left side of which is shown in Fig. 6(a). For such large core separations, linear coupling is very small, especially for short wavelengths, and all supermodes have essentially the same dispersion, which is that of an isolated core. Isolated core dispersion was thus used for the dispersion in the condition of Eq. (17), and the condition is satisfied at a wavelength of 950 nm, which is indicated by the vertical dashed line. This wavelength is in good agreement with the observed wavelength of the DW, as can be seen in Fig. 6(b), which shows the total spectrum as well as the outer-cores-only spectrum at a propagation distance of 8 cm.

After the emission of the DW in Figs. 4 and 5, the DW continues to propagate in the center core only, and it is completely absent from the outer cores. This is because the DW is at a short wavelength where the coupling between the cores is negligible, especially given that the core separation is as large as 25  $\mu\text{m}$ . The coupling length of this fiber, defined here as  $\pi/[2\kappa(\lambda)]$ , is shown in Fig. 7 together with the (separation-independent) nonlinear parameter  $\gamma(\lambda)$ . The coupling length gives the length scale over which coupling effects take place, and it can be seen to be orders of magnitude larger than the fiber length for wavelengths less than 1.3  $\mu\text{m}$ , which is why these wavelengths do not appreciably couple to the outer cores.

The intermediate-coupling regime breaks the general trend of the spectral width increasing with core separation. As can be seen in Fig. 3, there are clear peaks and valleys when core spacing is between 15  $\mu\text{m}$  and 20  $\mu\text{m}$  for peak powers larger than 10 kW. The peak at 15.5  $\mu\text{m}$  can be explained in terms of soliton supermode transitions [24]. The group velocities of supermodes depend on both the core separation and wavelength through their dependence on the coupling parameter  $\kappa(\omega)$ . It is therefore possible for two pulses at different wavelengths to copropagate

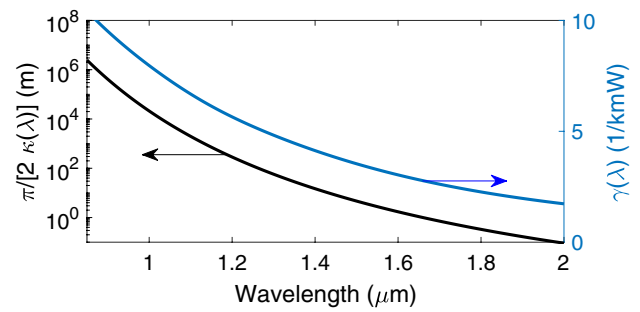


**Fig. 7.** Coupling length (left scale, logarithmic) and nonlinear parameter (right scale, linear) of the fiber, where the core separation is 25  $\mu\text{m}$ . The nonlinear parameter is independent of core separation.

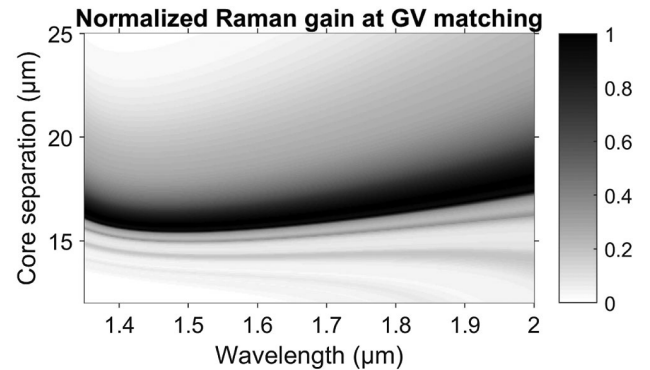


**Fig. 8.** Normalized Raman gain (color coded) at the group-velocity-matched wavelength in supermode *A* when the pump is in supermode *F*. The horizontal axis corresponds to the wavelength of the pump in *F* and the vertical axis to the core separation.

at the same group velocity, if they are in different supermodes. If the frequency separation required for group velocity matching happens to coincide with the peak of the Raman gain of silica at 13.2 THz and the two participating supermodes overlap spatially, Raman-induced power transfer can occur between them [24]. Figure 8 shows the normalized Raman gain experienced by a signal in supermode *A* that is group-velocity matched to a pump propagating in supermode *F* as a function of core separation and the wavelength of the pump in *F*. It can be seen that there is a narrow range of core separations around 16  $\mu\text{m}$ , where a signal in supermode *A* can be amplified by a pump pulse in *F* centered at 1.55  $\mu\text{m}$ . Furthermore, for core separations in this range, the Raman gain is fairly insensitive to variations in the wavelength of the pump pulse. This means that a pump pulse in *F* can keep transferring energy to a group-velocity-matched pulse in *A* even if the pump pulse changes its wavelength, e.g., due to soliton self-frequency shift.

The power transfer phenomenon between two supermodes is the multi-core equivalent of soliton self-mode conversion in step-index multi-mode fibers [5,6]. If the fiber is long enough, the supermode transition will be complete, and all of the energy from one soliton would transfer to the Stokes soliton at a longer wavelength in a different supermode. However, if the fiber ends before the process can complete, the output will include both the pump soliton and the Stokes soliton. It turns out that for a core separation of approximately 15.5  $\mu\text{m}$ , the midpoint of the

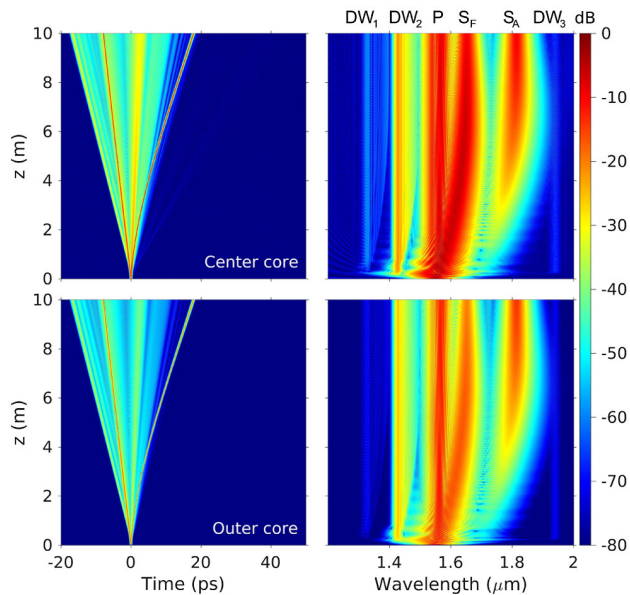


**Fig. 9.** Evolution of a 100 fs input pulse launched with 15 kW peak power into the center core of a seven-core fiber with 15.5  $\mu\text{m}$  core separation. The pump, solitons, and dispersive waves are labeled in the center-core spectrum. See [Visualization 3](#) for an animated spectrogram of this simulation.

supermode transition for a 15 kW input power is at a propagation distance of 10 m, which is the fiber length used here. This can be seen in Fig. 9, which shows the evolution of the 15 kW pulse in a fiber where the core separation is 15.5  $\mu\text{m}$ .

It can be seen in Fig. 9 that the output spectrum consists of three peaks of roughly equal power. The peak at 1.55  $\mu\text{m}$  (labeled P) is the remnants of the pump, the next one at 1.625  $\mu\text{m}$  (labeled  $S_F$ ) is the soliton in supermode  $F$ , and the peak at 1.81  $\mu\text{m}$  is the forming Stokes soliton in supermode  $A$  (labeled  $S_A$ ). The DWs are labeled  $DW_1$ ,  $DW_2$ , and  $DW_3$ . Because of the presence of multiple spectral peaks with roughly equal amplitudes, the spectral width as defined by the standard deviation is larger than for other core separations close to the 15.5  $\mu\text{m}$  value. For smaller core separations, the group velocity matching between supermodes  $A$  and  $F$  occurs for a frequency separation larger than the Raman gain bandwidth (see Fig. 8), and the power transfer between the participating solitons becomes inefficient. Consequently, the soliton in  $F$  has more energy than the Stokes soliton forming in  $A$  at the output of the fiber. Energy is therefore more concentrated in one part of the spectrum, and the width is smaller. For core separations slightly larger than 15.5  $\mu\text{m}$ , the Raman-induced energy transfer process becomes too efficient, and the soliton supermode transition will be nearly complete by the fiber output. Most of the energy will therefore be in the Stokes soliton in supermode  $A$ , and again the energy is concentrated in a smaller wavelength range, and the spectral width is decreased.

Although the solitons contain the majority of the total optical power in the simulation in Fig. 9, the DWs are clearly visible as well.  $DW_2$  at 1.425  $\mu\text{m}$  and  $DW_3$  at 1.93  $\mu\text{m}$  are in supermode  $A$ , and they are emitted by the soliton in supermode  $F$ . Again, their observed wavelengths match the predictions of the DW condition of Eq. (17).  $DW_1$  on the blue side is centered around

1.325  $\mu\text{m}$ , but does not fulfill the DW condition, and therefore its origins lie somewhere else. It can be seen in Fig. 9, and especially in the spectrogram animation ([Visualization 3](#)), that  $DW_1$  and  $DW_2$  are always generated at the same time and their spectra follow similar trajectories in the sense that both DWs gain more energy on their red sides as the soliton responsible for the generation of  $DW_2$  red shifts upon propagation. This indicates that the generation of  $DW_1$  is likely due to a four-wave mixing (FWM) process involving  $DW_2$  and one or both of the solitons  $S_A$  and  $S_F$ . The phase-matching condition for FWM is different from that of DW generation, and it is simply given by

$$\beta(\omega_1) + \beta(\omega_2) = \beta(\omega_3) + \beta(\omega_4), \quad (20)$$

where photons at  $\omega_1$  and  $\omega_2$  are destroyed, and photons at  $\omega_3$  and  $\omega_4$  are created. Energy has to be conserved as well, which yields the condition  $\omega_1 + \omega_2 = \omega_3 + \omega_4$ . Note that not all of the involved frequencies have to be different. The two FWM processes that are likely candidates for the origin of  $DW_1$  are the process where  $DW_2$  loses two photons, and one in  $DW_1$  and one in  $S_F$  are created, and the process where one photon from  $DW_2$  and one from  $S_F$  interact to produce one photon in  $DW_1$  and one in  $S_A$ . Figure 10 shows the observed peak wavelength of  $DW_1$  together with the wavelengths where the FWM phase-matching conditions would be fulfilled. The agreement is reasonable, such that an alternative explanation for the origin of  $DW_1$  seems unlikely.

Now looking back at the spectral widths shown in Fig. 3, the second peak in the intermediate-coupling region observed for higher peak powers is also explained by a double peak structure in the resulting output spectrum together with a slightly more intense DW emission. The difference between the supermode-transition peak and this peak is that the latter is observed only for high input powers, for which rapid spectral broadening occurs within the first tens of centimeters of propagation. The output spectrum is almost solely defined by the early stages of propagation for high input powers, and if the generated supercontinuum happens to have a double peak structure, where the two peaks have approximately equal energies, the spectrum will be wide. Between the second peak of the intermediate-coupling regime and the weak-coupling regime, the supercontinuum also forms within a short propagation distance, but the more red-shifted peak dominates and causes the spectral width to decrease before the weak-coupling regime. The supercontinuum is also formed within a short distance in the weak-coupling

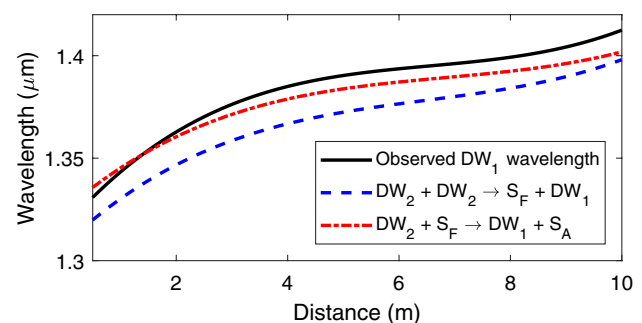


**Fig. 10.** Observed wavelength of  $DW_1$  in Fig. 9 (solid black line) and the wavelengths from the phase-matching condition for two FWM processes considered as candidates for the origin of  $DW_1$ .

regime (large core separations) but with the difference that the optical power is initially strongly confined in the center core. This causes the forming soliton to red shift rapidly, and it distances itself from the pump remnants in the spectral domain. Considerable energy is left in the pump remnants at  $1.55 \mu\text{m}$  as well, and the further the red shifting soliton is from the pump in the spectral domain, the larger becomes the standard deviation. This explains the monotonic increase in the spectral width with core separation in the weak-coupling region.

## 6. RESULTS FOR OUTER-CORE EXCITATION

We briefly discuss the case in which the input pulse is launched into one of the outer cores. Using an outer core as the input core excites at least five out of the seven supermodes shown in Fig. 1. Note that while every outer core is identical, we have fixed the orientation of supermodes *B*, *C*, *D*, and *E* in Fig. 1, which makes the number of excited supermodes dependent on which outer core is used as the input core. To keep the analysis as simple as possible, it is convenient to consider the core number 2 as the input core. In this case, supermodes *A*, *B*, *D*, *F*, and *G* are excited with relative energies of 11.5%, 33.3%, 33.3%, 5.2%, and 16.7%, respectively. Supermodes *C* and *E* are not symmetric with respect to the horizontal axis, and therefore they contain no optical power when the second core is the input core. In a perfect fiber, the fields in cores 3 and 7 would be identical at every stage of propagation, as would be the fields in cores 4 and 6.

Figure 11 shows the spectral widths of the supercontinua generated in fibers with various core separations when an outer core is used as the input core. It is similar to Fig. 3 with the only difference that the input pulse is launched in outer core 2 rather than the central core. However, there are two key differences. First, outer-core excitation leads to smaller spectral widths for small core separations. The reason for the smaller spectral width for small core separation (strong-coupling regime) is that the power is distributed among five supermodes, and hence the pulse splits into multiple daughter pulses that separate in time, which decreases the peak power of the pulse and hinders nonlinearities. This is clearly visible in Fig. 12, which shows the evolution of a 15 kW pulse in a fiber where the cores are separated by  $12 \mu\text{m}$ . Three different daughter pulse trajectories

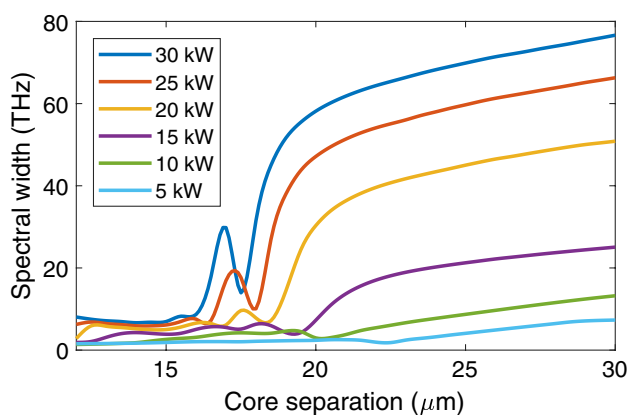


**Fig. 11.** Spectral widths of the supercontinua under conditions in Fig. 3 except that the input pulse is launched into the outer core 2.

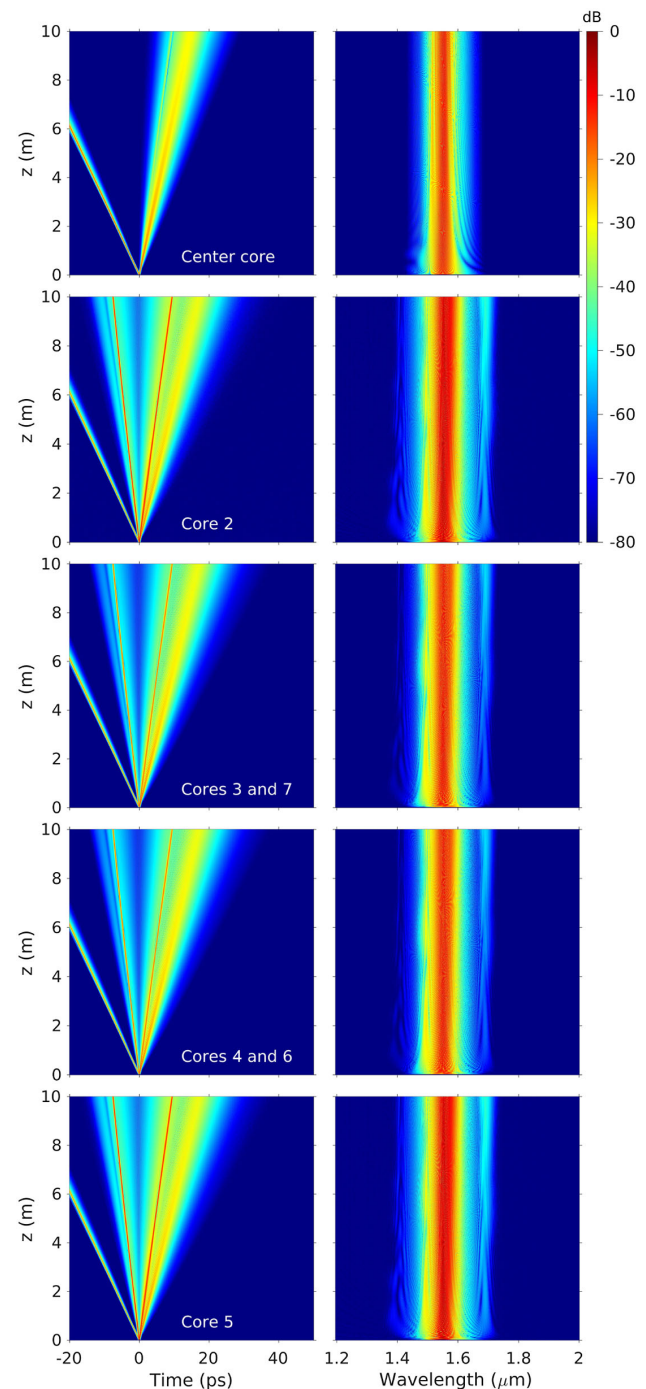


**Fig. 12.** Evolution of a 100 fs input pulse launched with 15 kW peak power into an outer core (core no. 2, see Fig. 1) of a seven-core fiber with  $12 \mu\text{m}$  core separation (strong-coupling regime).

can be identified, and none of the pulses is even strong enough to red shift.

Second, spectral widths are larger in Fig. 11 compared to Fig. 3 for large core separations. The explanation for this behavior lies in the fact that the center core is coupled to all outer cores, whereas any outer core has only three nearest neighbors. For large core separations, the coupling is initially weak but increases upon red shifting of the solitons. In the case of center-core excitation, the increasing coupling rapidly redistributes the

energy among all cores. In contrast, for outer-core excitation, the redistribution occurs over longer distances because the core is coupled to only three other cores. As a result, the pulse can red shift further, which increases the spectral width.

## 7. CONCLUSION

We studied supercontinuum generation in a hexagonal seven-core fiber and found that the output spectra were sensitive to the spacing among the seven cores. In addition to the dependence of supercontinuum generation on the parameters of the input pulse, such as its width and peak power, the results also depend on whether the pulse is launched into the central core or an outer core. The dynamics of supercontinuum generation were found to be heavily affected by the core separation, with larger core separations generally creating the broadest spectra. In all coupling regimes, the spectral broadening was found to be dominated by soliton formation and the associated red shift. For small core separations, the energy redistributes among different supermodes that separate in time, which results in decreased peak power and suppressed nonlinear effects. For large core separations, the coupling is weak, and the input pulse first behaves like a pulse in an isolated single-mode fiber and red shifts rapidly. As coupling between the cores increases with wavelength, the pulse eventually couples to the other cores, and the red shift stops as a result of the energy redistribution. In the intermediate-coupling regime, soliton supermode transitions were observed when the group velocity of two supermodes was matched for frequency separations near the Raman peak of silica (near 13.2 THz). The transitions are characterized by an abrupt spectral jump to longer wavelengths, which increases the spectral width of the resulting supercontinuum. Outer-core excitation was shown to result in narrower spectra in the strong-coupling regime but wider spectra in the weak-coupling regime, compared to using the center core as the input core. These differences were attributed to different group velocities of supermodes that split the pulse in time and to the faster energy redistribution for center-core excitation, as the center core is coupled to every other core of the fiber.

**Funding.** National Science Foundation (ECCS-1505636, ECCS-1933328).

## REFERENCES

- J. M. Dudley, G. Genty, and S. Coen, "Supercontinuum generation in photonic crystal fiber," *Rev. Mod. Phys.* **78**, 1135 (2006).
- W. H. Renninger and F. W. Wise, "Optical solitons in graded-index multimode fibres," *Nat. Commun.* **4**, 1719 (2013).
- K. Krupa, V. Couderc, A. Tonello, A. Picozzi, A. Barthélémy, G. Millot, and S. Wabnitz, "Spatiotemporal nonlinear dynamics in multimode fibers," in *Nonlinear Guided Wave Optics*, S. Wabnitz, ed. (IOP Science, 2014), Chap. 14.
- L. G. Wright, Z. M. Ziegler, P. M. Lushnikov, Z. Zhu, M. A. Eftekhar, D. N. Christodoulides, and F. W. Wise, "Multimode nonlinear fiber optics: massively parallel numerical solver, tutorial, and outlook," *IEEE J. Sel. Top. Quantum Electron.* **24**, 5100516 (2018).
- A. Antikainen, L. Rishøj, B. Tai, S. Ramachandran, and G. P. Agrawal, "Fate of a soliton in a high order spatial mode of a multimode fiber," *Phys. Rev. Lett.* **122**, 023901 (2019).
- L. Rishøj, B. Tai, P. Kristensen, and S. Ramachandran, "Soliton self-mode conversion: revisiting Raman scattering of ultrashort pulses," *Optica* **6**, 304–308 (2019).
- S. Mumtaz, R.-J. Essiambre, and G. P. Agrawal, "Reduction of nonlinear penalties due to linear coupling in multicore optical fibers," *IEEE Photon. Technol. Lett.* **24**, 1574–1576 (2012).
- T. Hayashi, Y. Tamura, T. Hasegawa, and T. Taru, "Record-low spatial mode dispersion and ultra-low loss coupled multi-core fiber for ultra-long-haul transmission," *J. Lightwave Technol.* **35**, 450–457 (2017).
- R. Ryf, N. K. Fontaine, S. H. Chang, J. C. Alvarado, B. Huang, J. Antonio-López, H. Chen, R.-J. Essiambre, E. Burrows, R. W. Tkach, R. Amezcua-Correa, T. Hayashi, Y. Tamura, T. Hasegawa, and T. Taru, "Long-haul transmission over multi-core fibers with coupled cores," in *European Conference on Optical Communication (ECOC)* (2017), paper M.2.E.1.
- R. Ryf, J. C. Alvarado-Zacarias, S. Wittek, N. K. Fontaine, R. Essiambre, H. Chen, R. Amezcua-Correa, H. Sakuma, T. Hayashi, and T. Hasegawa, "Coupled-core transmission over 7-core fiber," in *Optical Fiber Communication Conference Postdeadline Papers 2019* (Optical Society of America, 2019), paper Th4B.3.
- D. N. Christodoulides and R. I. Joseph, "Discrete self-focusing in nonlinear arrays of coupled waveguides," *Opt. Lett.* **13**, 794–796 (1988).
- A. M. Rubenchik, L. S. Chekhovskoy, M. P. Fedoruk, O. V. Shtyrina, and S. K. Turitsyn, "Nonlinear pulse combining and pulse compression in multi-core fibers," *Opt. Lett.* **40**, 721–724 (2015).
- S. M. Jensen, "The nonlinear coherent coupler," *IEEE J. Quantum Electron.* **18**, 1580–1583 (1982).
- A. M. Maier, "Optical transistors and bistable devices utilizing nonlinear transmission of light in systems with unidirectional coupled waves," *Kvant. Elektron. (Moscow)* **9**, 2296 (1982) [*Sov. J. Quantum Electron.* **12**, 1490 (1982)].
- A. V. Andrianov, N. A. Kalinin, M. Yu. Koptev, O. N. Egorova, A. V. Kim, and A. G. Litvak, "High-energy femtosecond pulse shaping, compression, and contrast enhancement using multicore fiber," *Opt. Lett.* **44**, 303–306 (2019).
- X. Fang, M. Hu, L. Huang, L. Chai, N. Dai, J. Li, A. Y. Tashchilina, A. M. Zheltikov, and C. Wang, "Multiwatt octave-spanning supercontinuum generation in multicore photonic-crystal fiber," *Opt. Lett.* **37**, 2292–2294 (2012).
- H. F. Wei, H. W. Chen, S. P. Chen, P. G. Yan, T. Liu, L. Guo, Y. Lei, Z. L. Chen, J. Li, X. B. Zhang, G. L. Zhang, J. Hou, W. J. Tong, J. Luo, J. Y. Li, and K. K. Chen, "A compact seven-core photonic crystal fiber supercontinuum source with 42.3 W output power," *Laser Phys. Lett.* **10**, 045101 (2013).
- P. Yan, G. Zhang, H. Wei, D. Ouyang, S. Huang, J. Zhao, K. Chen, J. Luo, and S. Ruan, "Double cladding seven-core photonic crystal fibers with different GVD properties and fundamental supermode output," *J. Lightwave Technol.* **31**, 3658–3662 (2013).
- H. Chen, H. Wei, T. Liu, X. Zhou, P. Yan, Z. Chen, S. Chen, J. Li, J. Hou, and Q. Lu, "All-fiber-integrated high-power supercontinuum sources based on multi-core photonic crystal fibers," *IEEE J. Sel. Top. Quantum Electron.* **20**, 0902008 (2014).
- X. Qi, S. Chen, A. Jin, T. Liu, and J. Hou, "Design and analysis of seven-core photonic crystal fiber for high-power visible supercontinuum generation," *Opt. Eng.* **54**, 066102 (2015).
- X. Luo, J. Peng, L. Cheng, L. Yang, N. Dai, H. Li, and J. Li, "Over octave-spanning supercontinuum generation in tapered seven-core photonic crystal fiber," *IEEE Photon. J.* **7**, 4501309 (2015).
- H. Wei, S. Chen, J. Hou, K. Chen, and J. Li, "A double-cladding seven-core photonic crystal fiber for hundred-watts-level all-fiber-integrated supercontinuum generation," *Chin. Phys. Lett.* **33**, 064202 (2016).
- X. Qi, S. Chen, Z. Li, T. Liu, Y. Ou, N. Wang, and J. Hou, "High-power visible-enhanced all-fiber supercontinuum generation in a seven-core photonic crystal fiber pumped at 1016 nm," *Opt. Lett.* **43**, 1019–1022 (2018).
- A. Antikainen and G. P. Agrawal, "Soliton supermode transitions and total red shift suppression in multi-core fibers," *Opt. Lett.* **44**, 4159–4162 (2019).
- T. Brabec and F. Krausz, "Nonlinear optical pulse propagation in the single-cycle regime," *Phys. Rev. Lett.* **78**, 3282–3285 (1997).

26. F. Poletti and P. Horak, "Description of ultrashort pulse propagation in multimode optical fibers," *J. Opt. Soc. Am. B* **25**, 1645–1654 (2008).
27. G. P. Agrawal, *Nonlinear Fiber Optics*, 5th ed. (Academic, 2013).
28. R. H. Stolen, J. P. Gordon, W. J. Tomlinson, and H. A. Haus, "Raman response function of silica-core fibers," *J. Opt. Soc. Am. B* **6**, 1159–1166 (1989).
29. I. H. Malitson, "Interspecimen comparison of the refractive index of fused silica," *J. Opt. Soc. Am.* **55**, 1205–1209 (1965).
30. R. Tewari and K. Thyagarajan, "Analysis of tunable single-mode fiber directional couplers using simple and accurate relations," *J. Lightwave Technol.* **4**, 386–390 (1986).
31. A. Sharma, S. I. Hosain, and A. K. Ghatak, "The fundamental mode of graded-index fibres: simple and accurate variational methods," *Opt. Quantum Electron.* **14**, 7–15 (1982).
32. F. M. Mitschke and L. F. Mollenauer, "Discovery of the soliton self-frequency shift," *Opt. Lett.* **11**, 659–661 (1986).
33. A. Antikainen, F. R. Arteaga-Sierra, and G. P. Agrawal, "Soliton dynamics in photonic-crystal fibers with frequency-dependent Kerr nonlinearity," *Phys. Rev. A* **95**, 033813 (2017).